



Smart multifunctional direct Z-scheme In_2S_3 @PCN-224 heterojunction for simultaneous detection and photodegradation towards antibiotic pollutants

Feng-Zao Chen^{a,b,c}, Yu-Jun Li^a, Mi Zhou^a, Xin-Xin Gong^a, Yuan Gao^a, Ge Cheng^c, Shi-Bin Ren^a, De-Man Han^{a,*}

^a School of Pharmaceutical Chemical and Engineering, Taizhou University, Taizhou 318000, China

^b Department of Chemistry, Zhejiang University, Hangzhou 310027, China

^c Taizhou Research Institute of Bio-medical and Chemical Industry Co., Ltd., Taizhou 318000, China

ARTICLE INFO

Keywords:

Multifunctional heterojunction
Z-scheme
 In_2S_3 @PCN-224
Photocatalysis
Fluorescence detection

ABSTRACT

Multifunctional heterojunctions, based on function- and structure-oriented material design and accurate synthesis, have emerged as an important platform in materials chemistry with great application prospects for solving practically complex science and engineering problems. Herein, a versatile Z-scheme In_2S_3 @PCN-224 platform, based on Zr-metal-organic framework (PCN-224) and In_2S_3 nanosheets, was constructed by solvothermal and hydrothermal methods. Benefited from the high efficiency in the photoinduced electron-hole separation of Z-scheme heterojunctions, high specific surface area of PCN-224 core, and good visible-light absorption of hydrophilic In_2S_3 shell, In_2S_3 @PCN-224 exhibited excellent performance in visible-light photocatalytic degradation towards tetracycline hydrochloride (TC). Furthermore, In_2S_3 @PCN-224 could be also used in fluorescence detection for TC with good analytical performance in terms of a large Stokes shift, fast response, and a low detection limit (55 nM). This work provides the inspiration for designing multifunctional heterojunctions, which will extend the boundary of "integration of diagnosis and treatment" in environmental management and control.

1. Introduction

Multifunctional materials are promising in solving practically complex science and engineering problems because of their ability to "kill two birds with one stone" [1–3]. One of the prescient moves from the perspective of advanced function design is to smartly integrate two or more kinds of functional materials into a novel composite. The use of antibiotics provides effective assistance for human health and development of animal husbandry, while there is growing concern about their overuse and inappropriate treatments. Particularly, tetracycline hydrochloride (TC), a broad-spectrum antibiotic with high physical-chemical stability but nonbiodegradability and lethality to most microorganisms, has been found in natural water and foods, posing a serious antibiotic pollution problem to the ecological environment as well as a threat to human health [4,5]. Despite many efforts to improve the analytical sensitivity or removal efficiency of TC, there are still significant difficulties in combining the two perfectly, with sensitive detection results guiding the subsequent process of antibiotic treatment, due to the smart material's diverse and high application requirements. Therefore, it is urgent and challenging to develop a multifunctional material for

effective detection (diagnosis) and elimination (treatment) of intractable TC contaminants simultaneously. Photocatalytic degradation has been widely considered an effective method to remove pollutants from aqueous environments. On this basis, ingenious design and development of recognition elements with highly visible-light response can help ones facilitate construction of a multifunctional platform to achieve the integrated "diagnosis and treatment" of target antibiotics. Even though this idea is full of expectations, it is still in the initial stage because the matching degree and interference between various components limit their functional integration.

Metal-organic frameworks (MOF), one of the most promising materials due to their tailorable structures and tunable properties, were spatially connected to inorganic metal clusters by organic ligands in a periodic manner [6–8]. MOF-type materials (e.g., Fe-MOF, Zr-MOF, Ti-MOF, Zn-MOF, Cu-MOF, and Lanthanide-MOF) enable a wide range of applications in environmental areas, not only as chemosensors for contaminants but also as adsorbents or photocatalysts [9–19]. Porphyrins play a key role in plant photosynthesis, both in capturing visible light and in electron transfer processes. Inspired by this natural process, we believe it is clever to select porphyrins as ligands to construct MOF

* Corresponding author.

<https://doi.org/10.1016/j.apcatb.2023.122517>

Received 30 November 2022; Received in revised form 11 January 2023; Accepted 22 February 2023

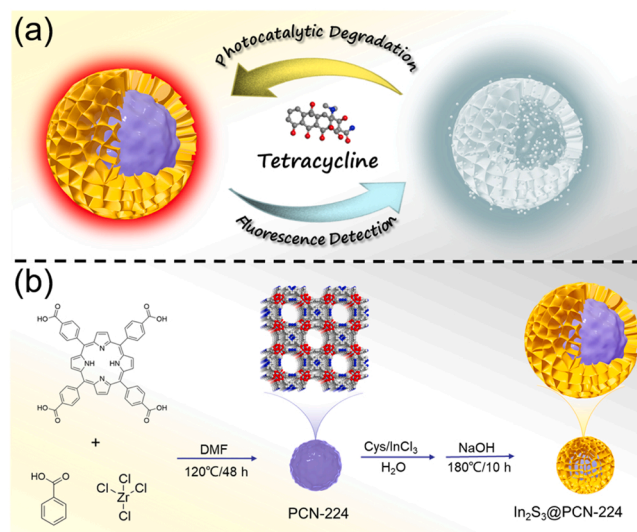
Available online 24 February 2023

0926-3373/© 2023 Elsevier B.V. All rights reserved.

materials for photocatalysis. More importantly, porphyrins and their derivatives not only have a strong visible-light response but also exhibit red fluorescence with a large Stokes shift, which provides a low signal background and interference for the sensitive detection of practical samples. PCN-224, a stable MOF composed of zirconium (Zr) clusters and porphyrin ligands, has been recently used in fluorescence analysis. For example, PCN-224-based materials have been performed to explore a pH-dependent sensor for 3-nitropropionic acid ratiometric detection [20], and due to the ligand-to-metal charge transfer, they were also used to monitor phosphate, relying on the existing linker-elimination strategy between porphyrin and phosphate [21]. Although PCN-224 derivatives have demonstrated high analytical performance for a variety of analytes, such as explosives [22], micro-RNA [23], molecules [24], and ions [25], their hydrophobic fluorescent reporter porphyrin and single-detecting function are insufficient to meet the demands of practical wastewater management. So far, the development of the multifunctional platform supplemented by the sensing performance of PCN-224 for exploiting the unique combination of accurate detection and fast adsorption/photodegradation towards TC contaminants has not yet been reported.

Heterojunction engineering is one of the most appealing approaches to developing advanced photocatalysts. The emergence of Z-scheme heterojunctions opens up new avenues to improve the photocatalytic activity because its unique dynamic process of charge carriers can greatly broaden the light response range, maintain the strong redox ability, and enhance the separation efficiency of photogenerated electron-hole pairs [26–30]. Various Z-scheme heterojunctions have been recently constructed in different applied fields, such as covalent-organic polymer/ZnIn₂S₄ [31], CoO/h-TiO₂ [32], g-C₃N₄/WO₃ [33], CdS/Fe₂O₃ [34], Bi₂S₃/Bi₂WO₆ [35], and SnS/g-C₃N₄ [36]. Metal sulfides, generally with good visible-light response and hydrophilicity, are widely used in the fields of photocatalysis, sensing, energy storage, and so on [37–39]. They have tunable energy bands and tailorable nanostructures such as nanospheres, nanorods, nanosheets, nanowires, etc. [40–43]. Among them, two-dimensional metal sulfide nanosheets have attracted much attention because of their large specific surface area, abundance of active sites, and optimized electron transfer path [44–46]. Despite these advantages, the fast recombination of electron-hole pairs still occurred under visible-light irradiation, which hampered its extensive applications in photocatalysis. As a result, combining two-dimensional metal sulfide with MOF materials to create a new type of heterojunction has significant future and application potential.

Herein, a novel multifunctional hierarchical Z-scheme core-shell nanostructure (In₂S₃@PCN-224) has been designed and constructed, composed of PCN-224 and In₂S₃ nanosheets with abundant reaction sites and visible-light capture capability, for simultaneous fluorescence detection and photodegradation of TC, as shown in Scheme 1a. The synthetic method involving successive solvothermal and hydrothermal treatments has been used to prepare the In₂S₃@PCN-224 hybrid photocatalysts, as illustrated in Scheme 1b. To obtain better analytical and removal performance against TC, the In₂S₃@PCN-224 composite was optimized by introducing different ratios of PCN-224 into In₂S₃. In the resultant nanostructure, PCN-224 can not only concentrate TC quickly but also serve as a recognition element and fluorescent reporter based on the interactions between the porphyrin ligands and the targeted TC. The flower-like structure of In₂S₃ nanosheet arrays, with an appropriate band gap, is the main photo-responsive element to photodegrade TC. Benefiting from the well-matched band gaps, the constructed In₂S₃@PCN-224 heterostructure struck an excellent balance with satisfactory light-harvesting capability and strong redox potential, compared with parent PCN-224 and In₂S₃ as the control, which achieved multifunctional applications in monitoring and removing TC contaminants. The fluorescence detection mechanism, the possible charge transfer pathway in In₂S₃@PCN-224 heterostructure, and the main photodegraded intermediates of TC have been further investigated. The scientific design and implementation of multifunctional MOF-based



Scheme 1. Schematic illustration of (a) multifunctional In₂S₃@PCN-224 for simultaneously detecting and photodegrading the targeted TC and (b) the synthetic process of In₂S₃@PCN-224.

heterostructure photocatalysts provided a promising model for the control and treatment of antibiotic residues in wastewater.

2. Experimental

2.1. Synthesis of In₂S₃@PCN-224 photocatalysts

In₂S₃@PCN-224 was synthesized by a one-step method similar to that of In₂S₃ (see in the Supporting Information). Specifically, PCN-224 in various ratios (30, 50, 70, and 100 mg) was added to the precursor solution of In₂S₃ and stirred for another 2 h before the heated treatment in an oven. The obtained In₂S₃@PCN-224 precipitates were washed with water/ethanol before drying at 60 °C for 12 h. The as-synthesized composites with different ratios of PCN-224 were labelled as ISP-30, ISP-50, ISP-70, and ISP-100, respectively.

2.2. Fluorescence detection towards TC

The ISP-70 powder (8 mg) was dispersed into deionized water (60 mL) to prepare a probe disperse liquid (0.133 mg/mL). For exploring the time-dependent fluorescence intensity changes, ISP-70 disperse liquid (200 µL) was added into TC solution (45 µM, 1800 µL), and the fluorescence spectra were recorded with an excitation wavelength of 420 nm. Under the optimized conditions, the probe liquid (200 µL) was then used to respond to TC solution (1800 µL) with different concentrations from 1 to 100 µM.

2.3. Adsorption and photodegradation towards TC

8 mg of photocatalysts (In₂S₃, PCN-224, and ISP) was placed into TC solution (25 mg/L, 60 mL) to evaluate their adsorption and photodegradation activities. The experiments were carried out in a cylindrical reactor containing condensed water to eliminate the effects of inevitably additional thermal. Adsorption was conducted in the dark for 60 min to ensure homogeneous dispersion of catalysts in the photocatalytic system and saturated adsorption towards TC. The photodegradation process occurred under visible-light irradiation stimulated by a 300 W Xenon lamp with a 420 nm filter. During the photodegradation process, a 3 mL reacted suspension was extracted every certain 5 min interval and centrifuged at 8000 rpm for 10 min in order to collect clear liquor for UV-vis spectrophotometer monitoring of residual TC concentrations at 357 nm. The removal efficiency (RE) of TC at a certain time was

calculated with the Eq. (1):

$$RE(\%) = C/C_0 \times 100\% \quad (1)$$

where C_0 and C (mg/L) represent the initial TC concentration (25 mg/L) and the TC concentration at a certain time, respectively. The detailed intermediates during the TC photodegrading process were analyzed by mass spectrometry.

3. Results and discussion

3.1. Characterization of photocatalysts

The crystallographic structures of In_2S_3 , PCN-224, and a series of ISP photocatalysts with different ratios of PCN-224 were characterized by powder X-ray diffraction (XRD) patterns. Fig. S1 shows that ISP photocatalyst composites exhibited similar characteristic diffraction peaks with parent In_2S_3 (JCPDS No. 32-0456), whose characteristic peaks at 27.5° , 32.9° , and 47.9° were indexed to the (311), (400), and (440) crystal faces, respectively [47,48]. The loading with various amounts of PCN-224 did not affect the crystal structure of In_2S_3 . The prominent characteristic diffraction peaks at 4.6° , 6.4° , 7.9° , 9.1° , 11.2° , and 13.7° were ascribed to the (002), (022), (222), (004), (224), and (006) lattice planes in the XRD pattern of PCN-224 [49]. However, no presence of

distinct characteristic diffraction peaks of PCN-224 can be observed in XRD patterns of ISP photocatalysts, which may be due to even a small amount of PCN-224.

Scanning electron microscopy (SEM) measurements and elemental mappings were applied to characterize the morphology and microstructure of photocatalysts. As shown in Fig. 1a, the parent PCN-224 exhibited an irregular blocky structure with a slightly wrinkled surface. Besides, a pure In_2S_3 microsphere with ca. 600 nm in diameter formed was also made up of several cross-linked petal-like nanosheets (Fig. 1b). To implant In_2S_3 onto the surface of PCN-224, a one-pot hydrothermal method was employed to give ISP-70 composite, which showed a regular spherical crystallite with the self-assembled In_2S_3 microspheres replaced by unfolded nanosheets vertically distributed on the surface of PCN-224 and the size of the crystallite around $2\text{ }\mu\text{m}$ in diameter (Fig. 1c). Elemental mappings of ISP-70 in Fig. 1d showed elements Zr, C, O, N, In, and S evenly scattered on ISP-70 photocatalyst, which revealed that both In and S elements on the surface of ISP-70 still maintained a consistent stoichiometric ratio with single In_2S_3 after hybridization with PCN-224, indicating the successful in-situ growth of In_2S_3 on the surface of PCN-224. Fig. S2 shows the corresponding high-resolution transmission electron microscopy (HRTEM) image of ISP-70. A lattice fringe with a distance of 0.268 nm can be found, agreeing well with the value of the (400) crystal plane in In_2S_3 . In addition, the

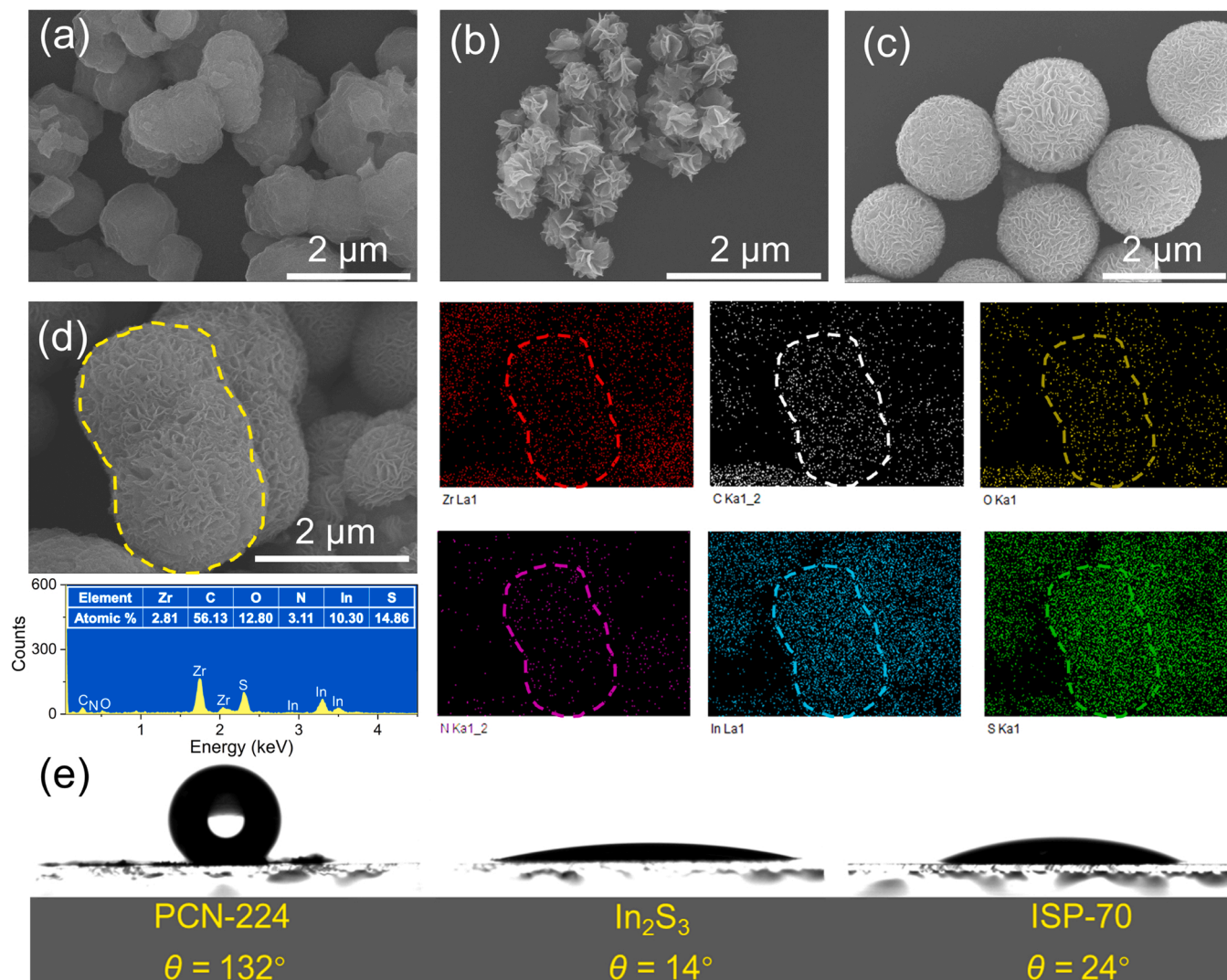


Fig. 1. Spectroscopic characterization and surface properties of photocatalysts: SEM images of (a) PCN-224, (b) In_2S_3 , and (c) ISP-70; (d) corresponding elemental mappings showing the distribution of Zr, C, O, N, In, and S in ISP-70 hybrid photocatalyst; (e) Water contact angles.

interface between PCN-224 and In_2S_3 can be clearly observed. This fact is of importance for effective charge delivery between the two components. To extend the photocatalytic degradation and fluorescence detection of as-prepared photocatalysts in aqueous systems, the prerequisites of good wettability and dispersion features of samples should be considered. Water contact angle measurements were carried out to evaluate the hydrophilicity of PCN-224, In_2S_3 , and ISP-70, as presented in Fig. 1e. PCN-224 with a large contact angle of about 132° revealed poor hydrophilicity due to its hydrophobic porphyrin moiety, while In_2S_3 with a small contact angle about 14° showed good hydrophilicity. The water contact angle of ISP-70, obtained from the conjugation of PCN-224 and In_2S_3 , was observed at about 24° ; such an obvious contact angle decreased when compared with that of PCN-224, illustrating that hydrophilic In_2S_3 gave the PCN-224 surface enhanced wettability. This made ISP-70 more available in the fields of photocatalytic degradation and fluorescence detection.

The chemical composition and bonding states of the ISP-70 hybrid photocatalyst were explored by X-ray photoelectron spectroscopy (XPS) using bare PCN-224 and In_2S_3 as the controlled samples. As depicted in Fig. 2a, the survey spectrum of ISP-70 showed the coexistence of N, O, C, Zr, In, and S elements derived from PCN-224 and In_2S_3 . The N 1s spectrum of ISP-70 in Fig. 2b could be deconvoluted into three peaks: the binding energies at 401.7, 399.5, and 397.8 eV ascribed to $-\text{N}^+\text{H}-$, $-\text{NH}-$, and $=\text{N}-$, respectively [50,51]. The high-resolution XPS spectra of the O element (Fig. 2c) illustrated the binding energies at 533.2, 531.9, and 530.7 eV that could be assigned to $-\text{OH}$, $\text{C}=\text{O}$, and $\text{Zr}-\text{O}-\text{Zr}$, respectively, which were consistent with the O 1s in PCN-224. The binding energy values of Zr $3d_{3/2}$ and Zr $3d_{5/2}$ were 185.3 and 182.9 eV, respectively, indicating the presence of Zr^{4+} ions in PCN-224 [52]. A 0.60 eV shift toward lower binding energy is observed for ISP-70 as compared to PCN-224 in Fig. 2d. Correspondingly, as for the S 2p region in Fig. 2e, the S $2p_{1/2}$ and S $2p_{3/2}$ peaks of In_2S_3 were situated at 162.4 and 161.3 eV, where the spin-orbit separation of S was 1.1 eV, thus asserting the valence of S element was -2 states. Compared with In_2S_3 , the characterized peaks of S $2p_{1/2}$ and S $2p_{3/2}$ in ISP-70 exhibited a positive shift to 162.6 and 161.5 eV, respectively. This may be due to the

higher ionization energy of sulfur than that of zirconium [53]. The signals centered at 452.2 eV and 444.7 eV (Fig. 2f) can be ascribed to In $3d_{3/2}$ and In $3d_{5/2}$, respectively. The acquired observations fully demonstrated the successful hybridization of In_2S_3 with PCN-224 to prepare the ISP-70 photocatalyst.

The isotherms and porous structures of PCN-224, In_2S_3 , and ISP-70 were confirmed by nitrogen adsorption-desorption characterizations at 77 K. Their corresponding specific surface areas and pore size distributions were obtained by the Brunauer-Emmett-Teller (BET) theory and Barrett-Joyner-Halenda (BJH) method, respectively. For the In_2S_3 isotherm in Fig. S3a, under the relative pressure of 0.45–0.9, the typical H3 hysteresis loop due to slit-like pores was observed, indicating the mesoporous property of bare In_2S_3 . PCN-224 gave the type I isotherm according to the International Union of Pure and Applied Chemistry (IUPAC) classification, as shown in Fig. S3b. The obtained ISP-70 photocatalyst with an apparent BET surface area of $151.62 \text{ m}^2/\text{g}$ was determined as a result of hybridizing In_2S_3 with PCN-224 when compared with PCN-224 ($S_{\text{BET}} = 534.73 \text{ m}^2/\text{g}$) and In_2S_3 ($S_{\text{BET}} = 62.04 \text{ m}^2/\text{g}$) (Fig. S3c), which was in favor of the practical adsorption and photodegradation towards targeted TC.

UV-vis diffuse reflectance spectra (UV-vis DRS) were used to explore the optical absorption characteristics of PCN-224, In_2S_3 , and a series of hybrid ISP photocatalysts, as shown in Fig. 3a. The pure In_2S_3 exhibited a clear absorption edge and the narrowest adsorption range at $\sim 550 \text{ nm}$. For bare PCN-224, an absorbed wavelength greater than 700 nm was recorded, indicating good visible-light absorption performance. With the increased amounts of PCN-224 in the ISP hybrids, the absorption edges of ISP composites shifted to longer wavelengths, which suggested that the ISP hybrids could harvest more effective visible light. As illustrated in Fig. 3b, the more detailed band gap energy values of PCN-224, In_2S_3 , ISP-30, ISP-50, ISP-70, and ISP-100 were estimated to be 1.78, 2.24, 2.19, 2.17, 2.07, and 1.93 eV, respectively, according to the Tauc plot Eq. (2),

$$(\alpha h\nu)^2 = A(h\nu - E_g) \quad (2)$$

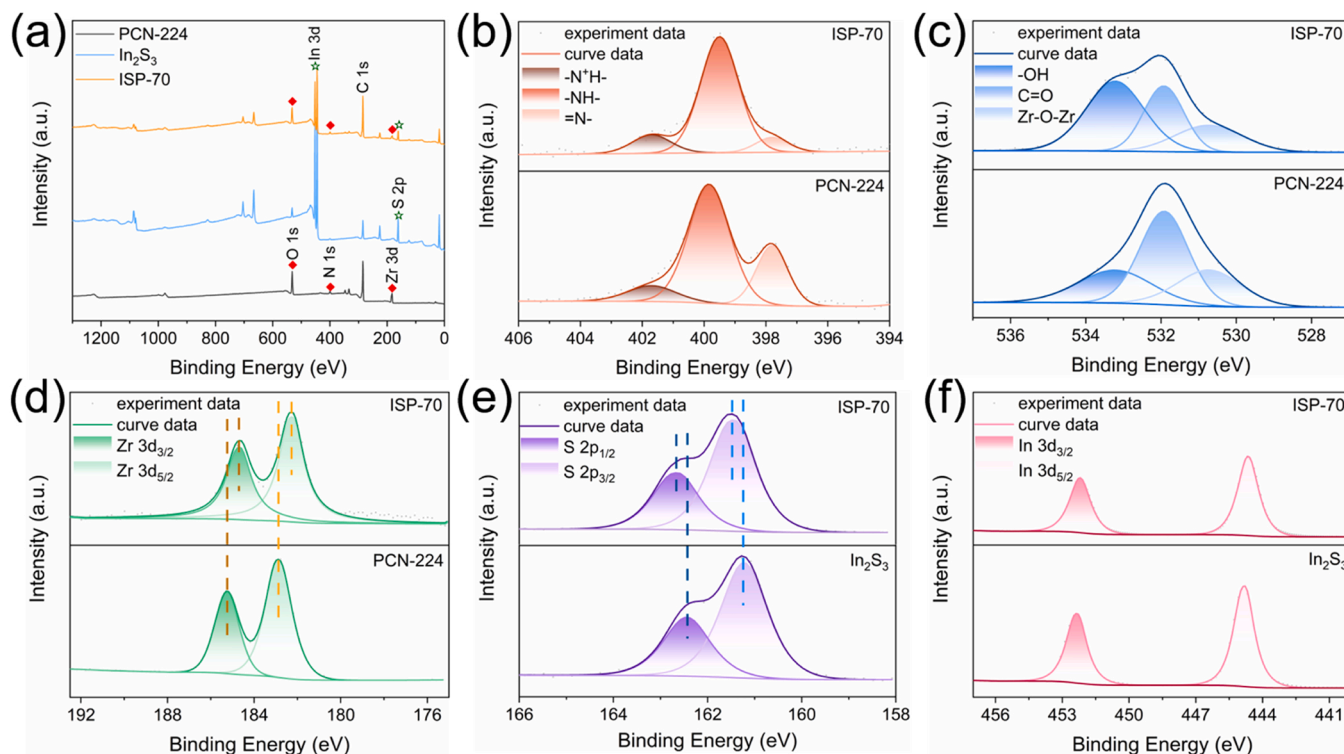


Fig. 2. XPS analysis of PCN-224, In_2S_3 , and ISP-70: (a) survey spectra, (b–f) high-resolution spectra of N 1s, O 1s, Zr 3d, S 2p, and In 3d, respectively.

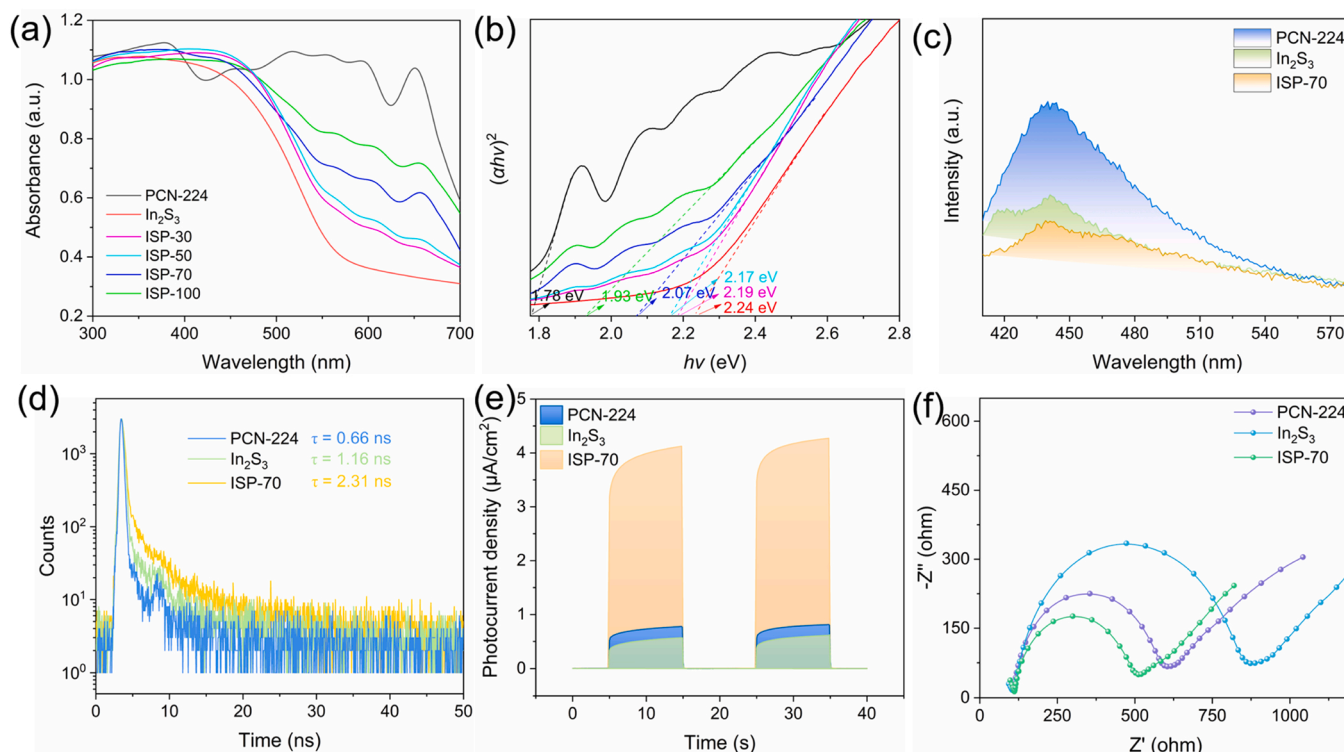


Fig. 3. (a) UV-vis DRS and (b) corresponding plots of $(\alpha h\nu)^2$ versus $h\nu$ for PCN-224, In_2S_3 , ISP-30, ISP-50, ISP-70, and ISP-100; (c) PL emission spectra, (d) time-resolved photoluminescence spectra, (e) photocurrent-time curves, and (f) EIS Nyquist plots of PCN-224, In_2S_3 , and ISP-70.

where α , h , A , and ν are the absorption coefficient, Planck constant, constant independent of energy, and light frequency, respectively.

In order to investigate the separation efficiency of photoinduced electron-hole pairs of the samples, photoluminescence (PL) measurements and transient photocurrent responses (I-t curves) were carried out. The PL emission spectra of PCN-224, In_2S_3 , and ISP-70 were obtained with an excitation wavelength of 385 nm (Fig. 3c). The strong PL intensity is generally associated with the fast recombination of charge carriers. It shows how the PL intensity of ISP-70 obviously decreased after the conjugation of PCN-224 and In_2S_3 , moreover, it demonstrates that the introduction of PCN-224 can offer more charge capture sites, thus inhibiting the recombination of electron-hole pairs. The fluorescence decay profiles (Fig. 3d) for PCN-224, In_2S_3 , and ISP-70 were measured with an excitation of 375 nm and detected at 440 nm. Through the Eq. (3),

$$\tau = (B_1\tau_1^2 + B_2\tau_2^2) / (B_1\tau_1 + B_2\tau_2) \quad (3)$$

the average life time (τ) of the photogenerated carriers can be illustrated. The calculated τ of bare PCN-224 and In_2S_3 were 0.66 ns and 1.16 ns, respectively. The short life time demonstrated that the photo-generated electrons of PCN-224 or In_2S_3 would rapidly recombine with holes. However, the average life time of ISP-70 showed further enhancement (2.31 ns). This result was attributed to the efficient carrier separation of ISP-70 heterojunction, which was in accordance with the PL results. The photoelectron-chemical responses were recorded in Na_2SO_4 electrolyte under intermittent visible-light irradiation. As illustrated in Fig. 3e, compared to the pure PCN-224 and In_2S_3 , the ISP-70 hybrid photocatalyst exhibited the largest photocurrent, which further verified the satisfactory separation efficiency of electron-hole pairs. In addition, electrochemical impedance spectroscopy (EIS) was further used to record the improvement in interfacial charge transfer behavior, as represented in Fig. 3f. The smallest semicircle radius of the ISP-70 EIS Nyquist plot could be found when PCN-224 and In_2S_3 were taken as the control samples, revealing a similar trend with the promoted

photocurrent.

3.2. Evaluation of photocatalytic activity

3.2.1. Photocatalytic degradation of TC

The photocatalytic performance was evaluated by TC degradation experiments in a cylindrical reactor with condensed water. Fig. S4 shows the changed UV-vis spectra related to TC adsorption and degradation over time. Due to the microporosity with high surface areas ($S_{\text{BET}} = 534.73 \text{ m}^2/\text{g}$), Fig. S4a shows that adsorption behavior in darkness played a key role in the removal process of TC contaminants from water over PCN-224. The semiconductor-like characteristics with a narrow bandgap contributed to PCN-224 exhibiting good photodegradation under simulated visible-light irradiation. Despite its lower surface area, the good adsorption effect of In_2S_3 was observed, as shown in Fig. S4b, as a result of the interaction between the exposed In(III) ions of In_2S_3 and the targeted TC. In addition, the proper positions of the conduction band (CB) and valence band (VB) intrinsic to In_2S_3 promoted its photocatalytic performance. Upon hybridizing PCN-224 with In_2S_3 , the as-obtained ISP-70 (Fig. S4c) exhibited a significant improvement in photodegradation of TC. A 1.7- or 2.0-fold increase in the photocatalytic efficiency of ISP-70 is achieved compared with In_2S_3 or PCN-224 within 40 min under visible-light irradiation, respectively, demonstrating the excellent simultaneous adsorption and degradation performance of ISP-70. Furthermore, all the ISP hybrid heterojunctions exhibited superior photocatalytic activity toward TC than that of pure PCN-224 and In_2S_3 , as shown in Fig. 4a. Although the different degradation tendency of TC over ISP heterojunctions was observed, it should be noted that the best degradation performance of ISP-70 indicated the optimal loading content of PCN-224 in hybrid photocatalysts. Fig. 4b shows the corresponding $-\ln(C/C_0)$ plots versus irradiation time with good linearity, which exhibits the TC degradation reaction conforming to the pseudo-first-order kinetic equation. For a clear illustration of the enhanced photocatalytic performance under visible-light irradiation, the photodegradation rate constants (κ) of all samples are represented in the

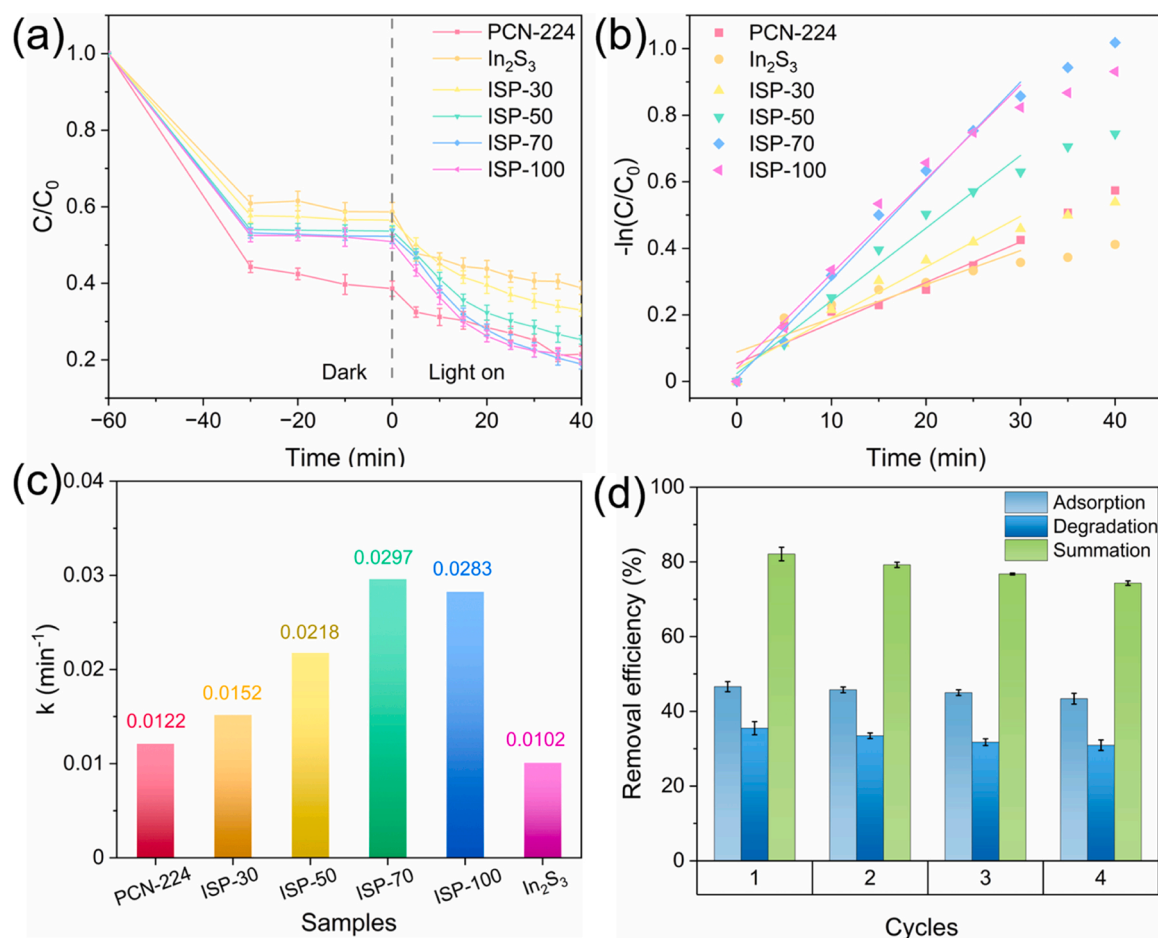


Fig. 4. Evaluation of adsorption and photocatalysis performance of PCN-224, In_2S_3 , ISP-30, ISP-50, ISP-70, and ISP-100 samples: (a) Photodegradation for TC under visible-light illumination; (b) Kinetic curves; (c) Reaction rate constants; and (d) Cycling runs over ISP-70.

schematic diagram in Fig. 4c. The as-prepared photocatalysts exhibited different degradation rates in the following order: ISP-70 > ISP-100 > ISP-50 > ISP-30 > PCN-224 > In_2S_3 . The rate constant of ISP-70 increased by a factor of about 2.9 and 2.4 compared with pristine In_2S_3 and PCN-224, respectively. In terms of practical stability and recyclability, the recycling experiments of as-prepared ISP-70 were carried out, and the results are shown in Fig. 4d, for example, ISP-70 still maintained more than 90% of its adsorption and degradation efficiencies after four successive photocatalytic reactions. It demonstrated that ISP-70 was a feasible photocatalyst for TC contaminant removal in wastewater treatment. To visually illustrate the stable microstructure of ISP-70 hybrids, SEM and XRD characterizations of fresh and used ISP-70 were performed. As shown in Fig. S5, the used samples still maintain a similar morphology to that of fresh ISP-70. Besides, Fig. S6 shows that the characteristic diffraction peaks of used ISP-70 were consistent with those of the fresh samples, and no additional diffraction peaks could be observed in the XRD pattern of ISP-70 after photocatalytic degradation. The above characterization results showed that the hybrid samples have good physical and chemical stability. Moreover, in order to exploit the photocatalytic performance of ISP-70 in complex water samples, we selected four different water samples from deionized water, lake water, river water, and tap water, respectively, to simulate natural water containing TC contaminant at a concentration of 25 mg/L. As shown in Fig. S7, the results of photodegradation tests showed that the removal efficiency of TC for these samples was in the range of 60–80% based on the adsorption and degradation performances even in the case of more complex natural water, thus illustrating the ISP-70/TC photocatalytic system's resistance to environmental disturbances.

3.2.2. Possible degradation pathway of TC

TC intermediates generated in the ISP-70 photocatalytic system during a 40 min degradation process were identified by mass spectrometry to provide deep insight into the degradation pathways. The main degradation process of TC with ISP-70 photocatalyst was proposed in Fig. S8 based on the single mass spectra shown in Fig. S9, apart from the characteristic peak of TC itself ($m/z = 444$), the information of byproducts including protonated intermediates and deprotonated intermediates [54,55]. The first degradation pathway showed the cleavage of the third ring in TC molecules and the fragmentation produced by the removal of two hydroxyl groups followed by the loss of N-dimethyl group and amide group to afford the final product (P1-P8-P9-P13). The second degradation pathway involved ring-opening and decarbonylation-induced molecule structure changes (P1-P2-P4). In the third degradation pathway (P1-P3-P12), the lower bond energy of C-N leading to the loss of the N-dimethyl group, and the cleavage of the third ring via radical attack along with oxidation and detachment of primary amine promoted the formation of the final product with m/z of 154. Additionally, the fragmentation of the intermediate with m/z of 383 occurred via the two cleavage pathways, such as the loss of water molecules and demethylation in the process of P1-P3-P5-P6-P7 and the elimination of hydroxyl groups, demethylation, and the cleavage of rings in the process of P1-P3-P5-P10-P11-P14, which was supported by the data of single mass spectra.

3.2.3. Possible photocatalytic mechanism of ISP-70

In order to ascertain the participation of free radicals during the process of photocatalytic degradation in the ISP-70/TC system, radical

scavenging experiments were carried out. When adding 1,4-benzoquinone (BQ), disodium ethylenediamine tetraacetic acid (EDTA), and 2-propanol (IPA), corresponding to the capturing agents for superoxide radicals ($\bullet\text{O}_2$), holes (h^+), and hydroxyl radicals ($\bullet\text{OH}$), to the ISP-70/TC photocatalytic system, the removal efficiencies of TC changed from 82% to about 20%, 44%, and 79%, respectively, as shown in Fig. 5a. Hence, the free radicals of $\bullet\text{O}_2$ and h^+ were crucial in this photodegradation system. Moreover, the electron-spin resonance (ESR) with 5,5-dimethyl-1-pyrroline N-oxide (DMPO) techniques were further used to verify the free radical generation. As revealed in Fig. 5b, with regard to ISP-70, almost no featured signals of DMPO- $\bullet\text{O}_2$ and DMPO- $\bullet\text{OH}$ can be recorded in darkness, indicating that visible-light illumination is necessary to produce the active species. After illumination, the strong ESR signal of DMPO- $\bullet\text{O}_2$ was found, whereas there were no characteristic signals of DMPO- $\bullet\text{OH}$, further verifying that photogenerated electrons can activate O_2 to produce $\bullet\text{O}_2$ as the main active species during TC photodegradation, which is consistent with radical scavenging experiments.

The Mott-Schottky plots of PCN-224 and In_2S_3 both showed positive slopes, implying n-type characteristics, as shown in Fig. 5c and d, and their derived flat-band potentials were determined as -0.63 and -0.42 V versus the Ag/AgCl electrode, respectively. Namely, the Fermi levels (E_f) of PCN-224 and In_2S_3 were calculated to be -0.43 and -0.22 V versus the normal hydrogen electrode (vs NHE), respectively. Generally, the difference between CB potential and E_f is approximately 0.1 V for n-type semiconductors. Thus, the CB potentials of PCN-224 and In_2S_3 were calculated as about -0.53 and -0.32 V, respectively. Then, in a combination of the band gap energies of PCN-224 (1.78 eV) and

In_2S_3 (2.24 eV), the VB potential could be estimated as 1.25 and 1.92 V, respectively. Based on the above analysis, the possible charge transfer pathway in the ISP hybrid photocatalyst was sketched in Scheme 2. Taking the CB/VB positions of PCN-224 and In_2S_3 into consideration, two possible photocatalytic mechanisms (Z-scheme and type II) in ISP-70 may be assumed. For the Z-scheme mechanism, following excitation with visible light, the photogenerated electron may migrate from the CB of In_2S_3 to the VB of PCN-224, resulting in effective charge separation and the maintenance of higher reduction/oxidation potentials in photocatalytic reactions. Under such a situation, the electrons on the CB of PCN-224 could react with O_2 to form $\bullet\text{O}_2$, and decompose the targeted TC. For the type II mechanism, the photogenerated electrons and holes were accumulated on the CB of In_2S_3 with a lower reduction potential and the VB of PCN-224 with a lower oxidation potential, respectively. The CB potential of In_2S_3 was more positive than that of $\text{O}_2/\bullet\text{O}_2$ (-0.33 V vs NHE) [56], indicating that the electrons accumulated on the CB of In_2S_3 could not reduce O_2 to $\bullet\text{O}_2$ free radicals. It was not beneficial to degradation reactions. Thus, it can be concluded that under visible-light irradiation, the charge migration pathway of ISP-70 composed of PCN-224 and In_2S_3 was the direct Z-scheme favored in the photocatalytic process. ISP-70's significantly improved photocatalytic performance was closely related to the successful construction of a Z-scheme heterojunction between PCN-224 and In_2S_3 .

3.3. Evaluation of fluorescence detection

As revealed in Fig. 6a, upon excitation at 420 nm, the respective In_2S_3 and TC exhibited very weak fluorescence, while PCN-224 emitted

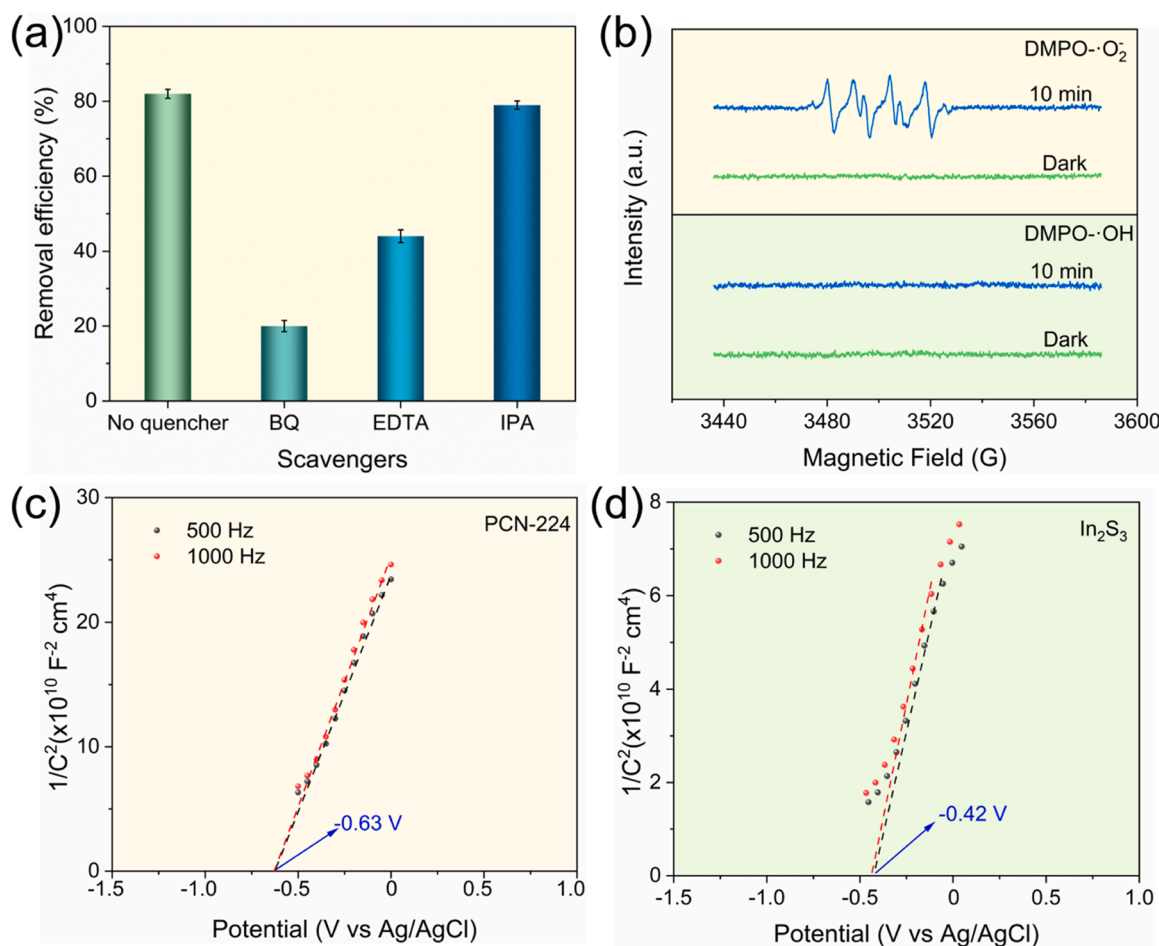
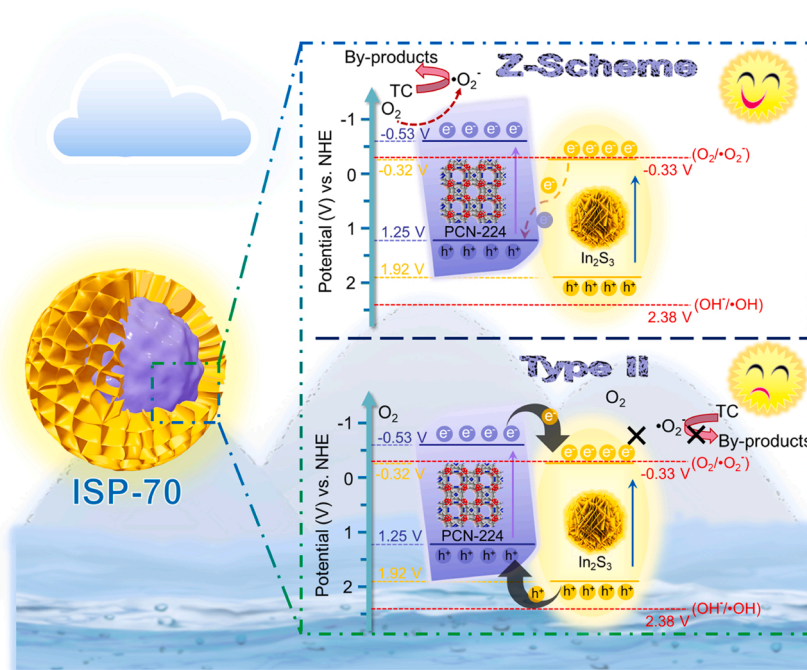


Fig. 5. (a) Radicals capturing experiments in the process of photodegradation for TC over ISP-70; (b) ESR spectra of ISP-70 in the dark or under visible-light irradiation (10 min): DMPO- $\bullet\text{O}_2$ in methanol dispersions and DMPO- $\bullet\text{OH}$ in aqueous dispersions; Mott-Schottky plots of (c) PCN-224 and (d) In_2S_3 .



Scheme 2. The possible photocatalytic mechanism of ISP-70 heterojunction.

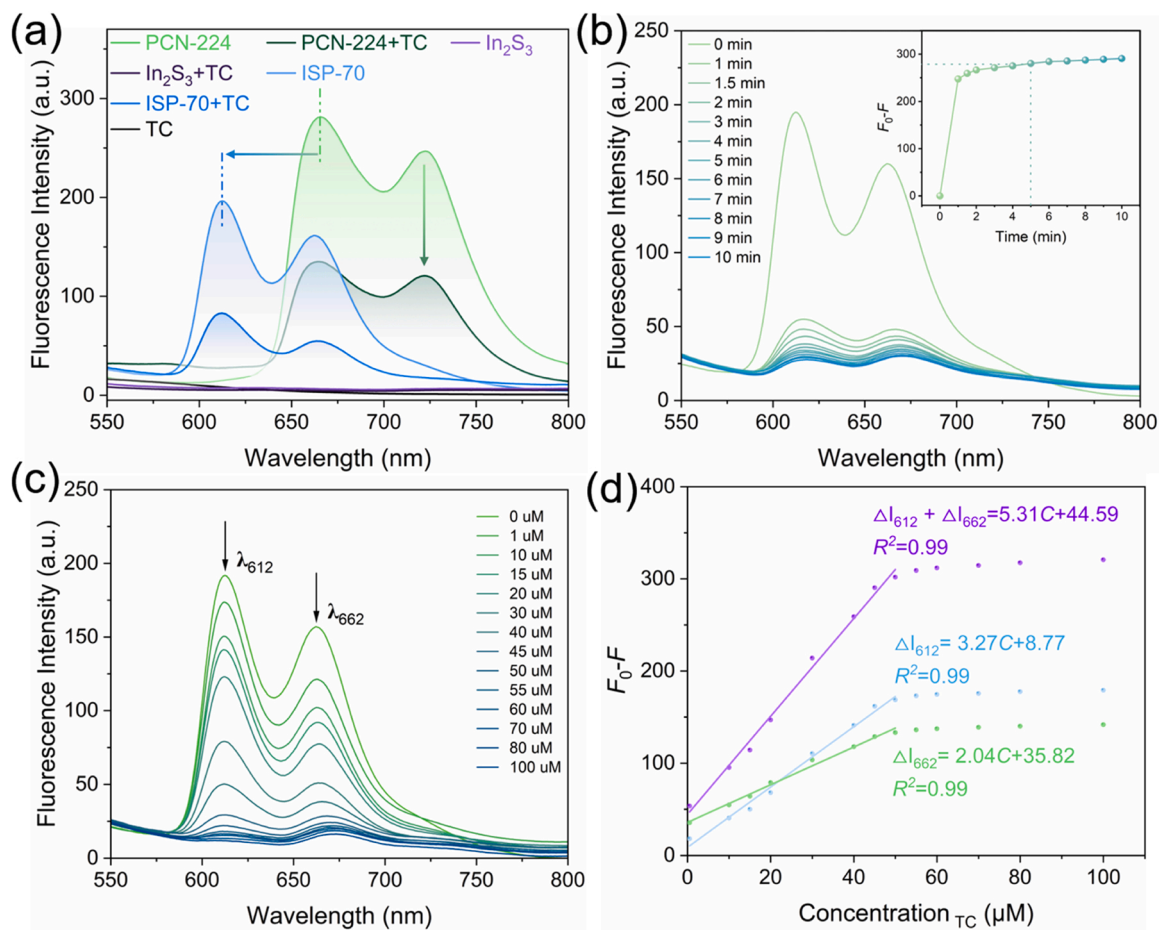


Fig. 6. Evaluation of fluorescence detection performance of ISP-70 (0.133 mg/mL) under an excitation wavelength of 420 nm: (a) Fluorescence emission spectra of PCN-224, In₂S₃, and ISP-70 before and after responding to TC; (b) Time-dependent fluorescence intensity; (c) TC concentration-dependent fluorescence emission spectra from 0 to 100 μM; (d) corresponding linear relationship between the change of fluorescence intensity before and after responding to TC (F_0-F) and TC concentrations.

strong fluorescence with a red emission at wavelengths of 665 nm and 722 nm and a large Stokes shift due to the organic porphyrin ligands. In the presence of TC, the In_2S_3 solution showed almost no fluorescence change. However, the fluorescence was sharply quenched when PCN-224 was treated with TC (30 μM), suggesting the strong interactions between TC and PCN-224. Concerning ISP-70, a similar decrease in fluorescence intensity was also observed upon detecting TC, confirming the capability for monitoring trace TC. Furthermore, a blue shift (~ 53 nm) in ISP-70 compared to PCN-224 may be attributed to PCN-224's changing microenvironment as a result of the introduction of In_2S_3 , as well as their close combination, which was consistent with the widening band gap from UV-vis DRS results in Fig. 3b. This did not affect the fluorescence detection for TC. As expected in Fig. 6b, in the presence of 45 μM of TC in the ISP-70 detecting system, the emission intensity obviously decreased with the increased response time and quickly reached the plateau in 5 min. Therefore, this response time was used in the next detection experiments. Under the optimized experimental conditions, the fluorescence signals of the as-developed ISP-70 sensing system towards TC with various concentrations from 0 to 100 μM were recorded in Fig. 6c. The fluorescence intensity gradually decreased as the TC concentration increased. Based on the decrement of fluorescence intensities centered at around 612 and 662 nm, two corresponding calibration curves that correlated well to the TC concentrations ranging from 1 to 50 μM showed reasonable correlation coefficients of about 0.99 (at 612 nm) and 0.99 (at 662 nm) in Fig. 6d. We further used the sum of the changed fluorescence intensities centered at both wavelengths as well as the increasing TC concentrations to derive the calibration curve with a larger slope. Notably, the result indicated ISP-70's higher sensitivity towards the targeted TC, and the limit of detection (LOD) was calculated as 55 nM by the formula $3\sigma/k$, where σ and k mean the standard deviation of blank tests and the slope of the derived calibration curve, respectively. Then, a detailed comparison of our research results with previous work in the detection and degradation of TC was listed in Table S1 in Supporting Information. The multifunctional ISP-70 outperformed the majority of reports. Subsequently, in order to test the feasibility of the control and treatment of antibiotic residue in wastewater based on this ISP-70/TC detection system, lake water, river water, and tap water were simply pretreated and used for the preparation of the water samples with the same concentration (45 μM) of TC. The relevant experiments were performed to give rise to fluorescence signals quenched remarkably upon responding TC, as shown in Fig. S10, confirming the significant feasibility of the ISP-70/TC detection system in complex environments. Thus, not only the satisfactory photocatalytic performance but also the fluorescence monitoring of the trace of TC have been integrated into ISP-70 in such a way, just like "killing two birds with one stone," which provided a new avenue for developing multifunctional nanomaterials.

4. Conclusions

In this work, a multifunctional hybrid photocatalyst, In_2S_3 @PCN-224, has been designed and synthesized under the practical demand guidance of "diagnosis and treatment" of antibiotic organic pollutants. The novel heterojunction was systematically characterized by X-ray diffraction (XRD), scanning electron microscopy (SEM) coupled with elemental mappings, X-ray photoelectron spectroscopy (XPS), the N_2 adsorption-desorption isotherm, UV-vis diffuse reflectance spectra (UV-vis DRS), photoluminescence (PL) measurements, and transient photocurrent responses (I-t curves). Different PCN-224 proportions were introduced to In_2S_3 @PCN-224 to obtain an optimized hybrid photocatalyst with improved TC adsorption, photodegradation, and fluorescence detection performances. The large specific surface area of PCN-224 and good hydrophilia of In_2S_3 endow hybrid photocatalysts with satisfactory adsorption ability. The improvement of visible-light-driven photocatalytic activity can be attributed to the newly formed direct Z-scheme heterojunction with effective spatial charge separation and well-

preserved strong redox ability. It was assumed that the fluorescence detection was due to the strong interaction between porphyrin ligands and targeted TC. The mechanisms of photocatalysis and fluorescence sensing have been systematically investigated, which fully demonstrates the feasibility and applicability of the multifunctional nanomaterials constructed by MOFs and semiconductors in the control and treatment of antibiotic residue in wastewater. We believe that future rational design and accurate nanomaterial synthesis can be envisioned to yield innovative multifunctional platforms with unique characteristic and extensive applications.

CRediT authorship contribution statement

Feng-Zao Chen: Data curation, Funding acquisition, Methodology, Writing – review & editing. **Yu-Jun Li:** Data curation, Formal analysis. **Mi Zhou:** Formal analysis. **Xin-Xin Gong:** Investigation. **Yuan Gao:** Conceptualization. **Ge Cheng:** Writing – review & editing. **Shi-Bin Ren:** Investigation. **De-Man Han:** Methodology, Supervision, Funding acquisition, Writing – review & editing.

Declaration of Competing Interest

The authors declare that they have no known competing financial interests or personal relationships that could have appeared to influence the work reported in this paper.

Data Availability

Data will be made available on request.

Acknowledgement

This work was financially supported by the National Natural Science Foundation of China (Nos. 21976129, 22204118), the Natural Science Foundation of Zhejiang Province (Nos. LQ22B050002), the Zhejiang Province Science Technology Planning Project (Nos. 2021C03023), and Zhejiang Provincial Science and Technology Innovation Program (New Young Talent Program) for College Students (Nos. 2022R436A010).

Appendix A. Supporting information

Supplementary data associated with this article can be found in the online version at doi:10.1016/j.apcatb.2023.122517.

References

- [1] Z. Zhu, D. Ng, H. Park, M. McAlpine, 3D-printed multifunctional materials enabled by artificial-intelligence-assisted fabrication technologies, *Nat. Rev. Mater.* 6 (2021) 27–47.
- [2] Z. Meng, K. Mirica, Covalent organic frameworks as multifunctional materials for chemical detection, *Chem. Soc. Rev.* 50 (2021) 13498–13558.
- [3] Y. Gao, J. Wu, J. Wang, Y. Fan, S. Zhang, W. Dai, A novel multifunctional p-type semiconductor@MOFs nanoporous platform for simultaneous sensing and photodegradation of tetracycline, *ACS Appl. Mater. Interfaces* 12 (2020) 11036–11044.
- [4] L. Xu, H. Zhang, P. Xiong, Q. Zhu, C. Liao, G. Jiang, Occurrence, fate, and risk assessment of typical tetracycline antibiotics in the aquatic environment: a review, *Sci. Total Environ.* 753 (2021), 141975.
- [5] F. Ahmadjokani, H. Molavi, S. Tajahmadi, M. Rezakazemi, M. Amini, M. Kamkar, O. Rojas, M. Arjmand, Coordination chemistry of metal-organic frameworks: Detection, adsorption, and photodegradation of tetracycline antibiotics and beyond, *Coord. Chem. Rev.* 464 (2022), 214562.
- [6] G. Cai, P. Yan, L. Zhang, H. Zhou, H. Jiang, Metal-organic framework-based hierarchically porous materials: synthesis and applications, *Chem. Rev.* 121 (2021) 12278–12326.
- [7] J. Qin, Y. Dou, F. Wu, Y. Yao, H. Andersen, C. Hélix-Nielsen, S. Lim, W. Zhang, In-situ formation of Ag_2O in metal-organic framework for light-driven upcycling of microplastics coupled with hydrogen production, *Appl. Catal. B* 319 (2022), 121940.
- [8] Z. Hu, Y. Wang, D. Zhao, The chemistry and applications of hafnium and cerium (IV) metal-organic frameworks, *Chem. Soc. Rev.* 50 (2021) 4629–4683.

- [9] C. Yan, J. Jin, J. Wang, F. Zhang, Y. Tian, C. Liu, F. Zhang, L. Cao, Y. Zhou, Q. Han, Metal-organic frameworks (MOFs) for the efficient removal of contaminants from water: Underlying mechanisms, recent advances, challenges, and future prospects, *Coord. Chem. Rev.* 468 (2022), 214595.
- [10] T. Hu, L. Tang, H. Feng, J. Zhang, X. Li, Y. Zuo, Z. Lu, W. Tang, Metal-organic frameworks (MOFs) and their derivatives as emerging catalysts for electro-Fenton process in water purification, *Coord. Chem. Rev.* 451 (2022), 214277.
- [11] S. Rojas, P. Horcajada, Metal-organic frameworks for the removal of emerging organic contaminants in water, *Chem. Rev.* 120 (2020) 8378–8415.
- [12] C. Du, Y. Zhang, Z. Zhang, L. Zhou, G. Yu, X. Wen, T. Chi, G. Wang, Y. Su, F. Deng, Y. Lv, H. Zhu, Fe-based metal organic frameworks (Fe-MOFs) for organic pollutants removal via photo-Fenton: a review, *Chem. Eng. J.* 431 (2022), 133932.
- [13] F. Chen, Y. Gao, Y. Li, W. Li, X. Wu, D. Han, W. Zhao, Photoelectrochemical detection of tetracycline with exceptional speediness, ultralow detection limit, and high selectivity, *Sens. Actuators B Chem.* 361 (2022), 131651.
- [14] D. Chen, Q. Bai, T. Ma, X. Jing, Y. Tian, R. Zhao, G. Zhu, Stable metal-organic framework fixing within zeolite beads for effectively static and continuous flow degradation of tetracycline by peroxydisulfate activation, *Chem. Eng. J.* 435 (2022), 134916.
- [15] Z. Wang, Z. Liu, J. Huang, Y. Chen, R. Su, J. He, G. Lv, B. Gao, W. Zhou, Y. Wang, Z. Wang, Q. Li, Zr₆O₈-porphyrinic MOFs as promising catalysts for the boosting photocatalytic degradation of contaminants in high salinity wastewater, *Chem. Eng. J.* 440 (2022), 135883.
- [16] Y. Wu, X. Li, H. Zhao, F. Yao, J. Cao, Z. Chen, D. Wang, Q. Yang, Core-shell structured Cu₂O@HKUST-1 heterojunction photocatalyst with robust stability for highly efficient tetracycline hydrochloride degradation under visible light, *Chem. Eng. J.* 426 (2021), 131255.
- [17] J. Li, C. Yu, Y. Wu, Y. Zhu, J. Xu, Y. Wang, H. Wang, M. Guo, F. Li, Novel sensing platform based on gold nanoparticle-aptamer and Fe-metal-organic framework for multiple antibiotic detection and signal amplification, *Environ. Int.* 125 (2019) 135–141.
- [18] X. Song, Y. Wang, T. Zhu, J. Liu, S. Zhang, Facile synthesis a novel core-shell amino functionalized MIL-125(Ti) micro-photocatalyst for enhanced degradation of tetracycline hydrochloride under visible light, *Chem. Eng. J.* 416 (2021), 129126.
- [19] G. Chen, S. He, G. Shi, Y. Ma, C. Ruan, X. Jin, Q. Chen, X. Liu, H. Dai, X. Chen, D. Huang, In-situ immobilization of ZIF-67 on wood aerogel for effective removal of tetracycline from water, *Chem. Eng. J.* 423 (2021), 130184.
- [20] X. Guo, N. Zhu, Y. Lou, S. Ren, S. Pang, Y. He, X. Chen, Z. Shi, S. Feng, A stable nanoscaled Zr-MOF for the detection of toxic mycotoxin through a pH-modulated ratiometric luminescent switch, *Chem. Commun.* 56 (2020) 5389–5392.
- [21] Y. Ma, Y. Zhang, X. Li, P. Yang, J. Yue, Y. Jiang, B. Tang, Linker-eliminated nano metal-organic framework fluorescent probe for highly selective and sensitive phosphate ratiometric detection in water and body fluids, *Anal. Chem.* 92 (2020) 3722–3727.
- [22] J. Yang, Z. Wang, K. Hu, Y. Li, J. Feng, J. Shi, J. Gu, Rapid and specific aqueous-phase detection of nitroaromatic explosives with inherent porphyrin recognition sites in metal-organic frameworks, *ACS Appl. Mater. Interfaces* 7 (2015) 11956–11964.
- [23] D. Wu, W. Dong, T. Yin, G. Jie, H. Zhou, PCN-224/nano-zinc oxide nanocomposite-based electrochemiluminescence biosensor for HPV-16 detection by multiple cycling amplification and hybridization chain reaction, *Sens. Actuators B: Chem.* 372 (2022), 132659.
- [24] M. Peng, G. Guan, H. Deng, B. Han, C. Tian, J. Zhuang, Y. Xu, W. Liu, Z. Lin, PCN-224/rGO nanocomposite based photoelectrochemical sensor with intrinsic recognition ability for efficient p-arsanilic acid detection, *Environ. Sci. Nano* 6 (2019) 207–215.
- [25] Z. Xu, Q. Li, Y. Wang, S. Yu, Y. Jiao, L. Wen, Y. Jiao, J. Tu, K. Xing, Y. Cheng, Target-triggered UCNP/Fe₃O₄@PCN-224 assembly for the detection of cadmium ions by upconversion fluorescence and magnetic relaxation switch dual-mode immunosensor, *Sens. Actuators B: Chem.* 377 (2023), 133037.
- [26] Y. Gao, M. Li, Y. Zeng, X. Liu, D. Tang, Tunable competitive absorption-induced signal-on photoelectrochemical immunoassay for cardiac troponin I based on z-scheme metal-organic framework heterojunctions, *Anal. Chem.* 94 (2022) 13582–13589.
- [27] X. Li, H. Sun, Y. Xie, Y. Liang, X. Gong, P. Qin, L. Jiang, J. Guo, C. Liu, Z. Wu, Principles, synthesis and applications of dual Z-scheme photocatalysts, *Coord. Chem. Rev.* 467 (2022), 214596.
- [28] P. Wang, S. Fan, X. Li, J. Wang, Z. Liu, C. Bai, M. Tade, S. Liu, Piezotronic effect and hierarchical Z-scheme heterostructure stimulated photocatalytic H₂ evolution integrated with C-N coupling of benzylamine, *Nano Energy* 89 (2021), 106349.
- [29] M. Ren, Y. Ao, P. Wang, C. Wang, Construction of silver/graphitic-C₃N₄/bismuth tantalate Z-scheme photocatalyst with enhanced visible-light-driven performance for sulfamethoxazole degradation, *Chem. Eng. J.* 378 (2019), 122122.
- [30] S. Zhou, Y. Wang, K. Zhou, D. Ba, Y. Ao, P. Wang, In-situ construction of Z-scheme g-C₃N₄/WO₃ composite with enhanced visible-light responsive performance for nitenpyram degradation, *Chin. Chem. Lett.* 32 (2021) 2179–2182.
- [31] C. Cui, X. Zhao, X. Su, N. Xi, X. Wang, X. Yu, X. Zhang, H. Liu, Y. Sang, Porphyrin-based donor-acceptor covalent polymer/ZnIn₂S₄ Z-scheme heterostructure for efficient photocatalytic hydrogen evolution, *Adv. Funct. Mater.* 32 (2022) 2208962.
- [32] X. Chen, B. Sun, J. Chu, Z. Han, Y. Wang, Y. Du, X. Han, P. Xu, Oxygen vacancy-induced construction of CoO/h-TiO₂ Z-scheme heterostructures for enhanced photocatalytic hydrogen evolution, *ACS Appl. Mater. Interfaces* 14 (2022) 28945–28955.
- [33] R. Shen, L. Zhang, N. Li, Z. Lou, T. Ma, P. Zhang, Y. Li, X. Li, W-N bonds precisely boost Z-scheme interfacial charge transfer in g-C₃N₄/WO₃ heterojunctions for enhanced photocatalytic H₂ evolution, *ACS Catal.* 12 (2022) 9994–10003.
- [34] X. Liu, D. Dai, Z. Cui, Q. Zhang, X. Gong, Z. Wang, Y. Liu, Z. Zheng, H. Cheng, Y. Dai, B. Huang, P. Wang, Optimizing the reaction pathway by active site regulation in the CdS/Fe₂O₃ Z-scheme heterojunction system for highly selective photocatalytic benzylamine oxidation integrated with H₂ production, *ACS Catal.* 12 (2022) 12386–12397.
- [35] Y. Cheng, J. Chen, P. Wang, W. Liu, H. Che, X. Gao, B. Liu, Y. Ao, Interfacial engineering boosting the piezocatalytic performance of Z-scheme heterojunction for carbamazepine degradation: Mechanism, degradation pathway and DFT calculation, *Appl. Catal., B* 317 (2022), 121793.
- [36] H. Omr, R. Putikam, M. Hussien, A. Sabbah, T. Lin, K. Chen, H. Wu, S. Feng, M. Lin, H. Lee, Design of sculptured SnS/g-C₃N₄ photocatalytic nanostructure for highly efficient and selective CO₂ conversion to methane, *Appl. Catal., B* 324 (2023), 122231.
- [37] Y. Liu, C. Chen, Y. He, Z. Zhang, M. Li, C. Li, X. Chen, Y. Han, Z. Shi, Rich indium-vacancies In₂S₃ with atomic p-n homojunction for boosting photocatalytic multifunctional properties, *Small* 18 (2022) 2201556.
- [38] J. Hu, M. Lu, F. Chen, H. Jia, H. Zhou, K. Li, X. Zeng, W. Zhao, P. Lin, Multifunctional hydrogel hybrid-gated organic photoelectrochemical transistor for biosensing, *Adv. Funct. Mater.* 32 (2022) 2109046.
- [39] P. Kumar, W. Wahyudi, A. Sharma, Y. Yuan, G. Harrison, M. Gedda, X. Wei, A. El-Labban, S. Ahmad, V. Kumar, V. Tung, T. Anthopoulos, Bismuth-based mixed-anion compounds for anode materials in rechargeable batteries, *Chem. Commun.* 58 (2022) 3354–3357.
- [40] X. Qian, H. Liu, J. Yang, H. Wang, J. Huang, C. Xu, Co-Cu-WS_x ball-in-ball nanospheres as high-performance Pt-free bifunctional catalysts in efficient dye-sensitized solar cells and alkaline hydrogen evolution, *J. Mater. Chem. A* 7 (2019) 6337–6347.
- [41] M. Zhang, X. Chen, X. Jiang, J. Wang, L. Xu, J. Qiu, W. Lu, D. Chen, Z. Li, Activate Fe₃S₄ nanorods by Ni doping for efficient dye-sensitized photocatalytic hydrogen production, *ACS Appl. Mater. Interfaces* 13 (2021) 14198–14206.
- [42] Y. Gao, J. Wu, J. Wang, N. Yan, N. Ma, W. Dai, Design and in situ synthesis of ZnInS@ZIF-8 nanofilms multifunctional nanocomposite: a case application for simultaneous fluorescent sensing and enhanced photocatalytic performance toward antibiotic, *Microporous Mesoporous Mater.* 315 (2021), 110916.
- [43] S. Foley, H. Geaney, G. Bree, K. Stokes, S. Connolly, M. Zaworotko, K. Ryan, Copper Sulfide (Cu₂S) Nanowire-in-carbon composites formed from direct sulfurization of the metal-organic framework HKUST-1 and their use as Li-ion battery cathodes, *Adv. Funct. Mater.* 28 (2018) 1800587.
- [44] Q. Chen, X. Chen, Q. Jiang, Z. Zheng, Z. Song, Z. Zhao, Z. Xie, Q. Kuang, Constructing oxide/sulfide in-plane heterojunctions with enlarged internal electric field for efficient CO₂ photoreduction, *Appl. Catal. B* 297 (2021), 120394.
- [45] F. Chen, Y. Zhu, D. Han, H. Chen, Three-dimensional ZnInS nanoflakes/carbon fiber frameworks for biocatalytic precipitation-based photoelectrochemical immunoassay, *ACS Appl. Bio Mater.* 3 (2020) 1761–1768.
- [46] L. Meng, D. Rao, W. Tian, F. Cao, X. Yan, L. Li, Simultaneous manipulation of O-doping and metal vacancy in atomically thin Zn₁₀In₁₆S₃₄ nanosheet arrays toward improved photoelectrochemical performance, *Angew. Chem. Int. Ed.* 57 (2018) 16882–16887.
- [47] H. Wang, X. Yuan, Y. Wu, G. Zeng, H. Dong, X. Chen, L. Leng, Z. Wu, L. Peng, In situ synthesis of In₂S₃@MIL-125(Ti) core-shell microparticle for the removal of tetracycline from wastewater by integrated adsorption and visible-light-driven photocatalysis, *Appl. Catal., B* 186 (2016) 19–29.
- [48] Y. Pi, S. Jin, X. Li, S. Tu, Z. Li, J. Xiao, Encapsulated MWCNT@MOF-derived In₂S₃ tubular heterostructures for boosted visible-light-driven degradation of tetracycline, *Appl. Catal. B* 256 (2019), 117882.
- [49] X. Liu, W. Qi, Y. Wang, D. Lin, X. Yang, R. Su, Z. He, Rational design of mimic multienzyme systems in hierarchically porous biomimetic metal-organic frameworks, *ACS Appl. Mater. Interfaces* 10 (2018) 33407–33415.
- [50] B. Wang, S. Liu, L. Liu, W. Song, Y. Zhang, S. Wang, Z. Han, MOF/PEDOT/HPMo-based polycrystalline hierarchical hollow micro-vesicles for high performance flexible supercapacitors, *J. Mater. Chem. A* 9 (2021) 2948–2958.
- [51] H. Liu, J. Zhang, D. Ao, Construction of heterostructured ZnIn₂S₄@NH₂-MIL-125 (Ti) nanocomposites for visible-light-driven H₂ production, *Appl. Catal. B* 221 (2018) 433–442.
- [52] L. Wang, P. Jin, J. Huang, H. She, Q. Wang, Integration of copper(II)-porphyrin zirconium metal-organic framework and titanium dioxide to construct Z-scheme system for highly improved photocatalytic CO₂ reduction, *ACS Sustain. Chem. Eng.* 7 (2019) 15660–15670.
- [53] Y. Liu, C. Chen, Y. He, Z. Zhang, M. Li, C. Li, X. Chen, Y. Han, Z. Shi, Rich indium-vacancies In₂S₃ with atomic p-n homojunction for boosting photocatalytic multifunctional properties, *Small* 18 (2022) 2201556.
- [54] B. Gao, S. Dong, J. Liu, L. Liu, Q. Feng, N. Tan, T. Liu, L. Bo, L. Wang, Identification of intermediates and transformation pathways derived from photocatalytic degradation of five antibiotics on ZnIn₂S₄, *Chem. Eng. J.* 304 (2016) 826–840.
- [55] A. Bembibre, M. Benamara, M. Hjiri, E. Gómez, H. Alamri, R. Dhahri, A. Serrà, Visible-light driven sonophotocatalytic removal of tetracycline using Ca-doped ZnO nanoparticles, *Chem. Eng. J.* 427 (2022), 132006.
- [56] L. Jiang, X. Yuan, G. Zeng, J. Liang, X. Chen, H. Yu, H. Wang, Z. Wu, J. Zhang, T. Xiong, In-situ synthesis of direct solid-state dual Z-scheme WO₃/g-C₃N₄/Bi₂O₃ photocatalyst for the degradation of refractory pollutant, *Appl. Catal. B* 227 (2018) 376–385.